

Multifunctional Halloysite-Glutathione Nanocomposite for Solar CO₂ Conversion and Pollutant Sensing

Erika Saccullo, Angelo Ferlazzo, Giusy Dativo, Roberto Fiorenza, Giulia Sambataro, Elena Bruno, Antonino Gulino, Antonio Rescifna, Vincenzo Patamia,* and Giuseppe Floresta*



Cite This: *ACS Appl. Nano Mater.* 2026, 9, 3941–3952



Read Online

ACCESS |

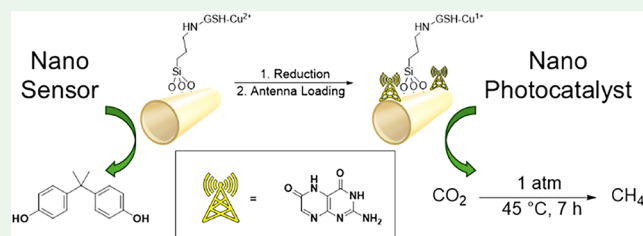
Metrics & More

Article Recommendations

Supporting Information

ABSTRACT: This study presents a highly sustainable nanocomposite platform for dual applications in both photocatalysis and sensing. The nanomaterial is synthesized via a green process using natural, readily available components, including halloysite nanotubes (HNTs), glutathione (GSH), and xanthopterin, utilizing copper ions (Cu^{1+}) as the catalytically active species. The synthesis, which exclusively uses green solvents like tetrahydropyran (THP) and water, involves functionalizing HNTs with (3-aminopropyl)-triethoxysilane (APTES), followed by the attachment of GSH as a chelating agent for Cu^{1+} . Finally, xanthopterin is loaded to act as a light-harvesting antenna. Fourier-transform infrared (FT-IR) spectroscopy and thermogravimetric analysis (TGA) confirmed the successful functionalization and composition. Scanning electron microscopy (SEM) and energy-dispersive X-ray (EDX) analysis validated the material's morphology and elemental composition. The resulting nanocomposite, HNT-NH₂-GSH-Cu¹⁺-X, demonstrated a remarkable synergistic effect, achieving a CO₂ conversion of 42.2% and a high (86.1%) CH₄ selectivity. Furthermore, the HNT-GSH-Cu²⁺ nanocomposite exhibited excellent electrochemical sensing capabilities for bisphenol A, with a low limit of detection (LOD) of 0.022 μM and a high sensitivity of 5.098 $\mu\text{A } \mu\text{M}^{-1}\cdot\text{cm}^{-2}$. The work successfully demonstrates the creation of a sustainable, multifunctional nanomaterial that addresses critical environmental challenges by combining efficient solar fuel production with highly sensitive pollutant detection.

KEYWORDS: HNT, nanotube, chelating agent, bisphenol A, CO₂ photoconversion, electrochemical nanosensor



1. INTRODUCTION

Developing new multifunctional nanomaterials is a critical challenge in addressing global issues such as sustainability and environmental protection.^{1,2} Systems capable of performing multiple tasks simultaneously, such as the photoconversion of CO₂ to methane and the detection of pollutants like bisphenol A, offer integrated, efficient solutions to both energy and environmental crises. Indeed, the possibility of producing solar fuels, such as methane, from CO₂ aligns with current calls for the development of a sustainable, nonfossil-fuel-based carbon economy. These solar fuels could be used for the synthesis of strategic chemicals or, if used in combustion processes, the emitted CO₂ could be balanced with the starting material used to produce the same solar fuels, enabling high-value-added products from a greenhouse gas with zero-carbon-emission processes. The importance of this work is underscored by the need to develop such systems sustainably, using green solvents and materials derived from renewable natural resources.

In this context, the use of sustainable nanomaterials, such as natural polysaccharides (cellulose, chitosan, and alginic acid) and natural clays, is transforming catalysis and sensing. These nanomaterials offer eco-friendly alternatives to synthetic compounds due to their abundance, biodegradability, and biocompatibility.^{3,4} Their matrices are often integrated with

chelating agents that bind metal ions, creating hybrid systems with unique functionalities.^{5–7} In catalysis, polysaccharides and halloysite nanotubes (HNTs) serve as versatile supports for immobilizing metal catalysts⁸ (e.g., palladium or copper nanoparticles) via chelating groups.⁹ This approach not only enhances catalyst stability but also facilitates its recovery and reuse, significantly reducing costs and environmental impact.

In sensing, the ability to chelate metal ions enables the development of highly selective and sensitive sensors.^{10–12} Their functionality is based on the change in the material's optical or electrochemical properties when an analyte binds to the chelating agent.^{13,14}

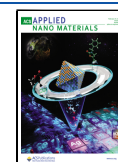
The choice between using HNTs and glutathione (GSH) is particularly significant. HNTs, natural clay minerals with tubular structures, provide a versatile scaffold that supports catalytically active agents.^{9,15–17} Thanks to their high surface area and stability, HNTs are also ideal for immobilizing

Received: December 23, 2025

Revised: February 6, 2026

Accepted: February 10, 2026

Published: February 14, 2026



receptors in electrochemical sensors, thereby improving their selectivity and sensitivity toward specific analytes such as organic pollutants, metal ions, and biomarkers.^{18–20}

GSH, a natural tripeptide, acts as a reducing and stabilizing agent for nanoparticles, a crucial aspect of their catalytic activity.^{21–23} In the field of sensing, GSH's thiol group offers highly specific recognition sites with a strong affinity for heavy metal ions (e.g., mercury or cadmium) and other pollutants.^{24,25} This property enables the creation of sensors with exceptional sensitivity for the detection of environmental contaminants.

By combining these two materials via a green synthesis route, this work aims to create a new, multifunctional nanoplatform that is not only effective for critical applications but also prepared in accordance with environmental sustainability principles. Despite the low copper content, this composite can function as an electrochemical nanosensor for bisphenol A. In the presence of an antenna of natural origin, it is also capable of converting CO₂ into CH₄ photochemically. Indeed, rather than the most commonly used and critical noble metals, the choice of copper as the photocatalytically active species is a more sustainable and green approach to producing solar fuels from CO₂, as copper is economical and not critical. Furthermore, particularly the cuprous ion, Cu (I), as reported in the literature, favors the selective CO₂ reduction^{9,26–28} into methane.

2. MATERIALS

2.1. General Information

All chemicals were purchased from Merck and VWR. Halloysite (HNT, cat. no. 685445), CuCl₂ (powder, 99%). Data for this article, including SEM-EDS, TGA, IR, and Electrochemical data are available at zenodo.org at [https://zenodo.org/records/17276779?token=eyJhbGciOiJIUzUxMiJ9.eyJpZCI6IjNhMzdmYmE3LTRhNjUtdmM4MS1iZTlhLTczOTg4MmQyZmRhZiIsImRhdGEiOnt9LCJyYW5kb20iOiJkODAsZmRkMTRhNjQyMzE3ZDAXYWY3MDFkOTgyNzAzYiJ9.D3pB5oTMRSCgzMARKuKdXDsvU11X7UXSWiZceoeNYcd7kqd1h7MYVlyDjiUdFX4PK0X0KNIjFoTXdSeC5yx4hA\(10.5281/zenodo.17276778\).](https://zenodo.org/records/17276779?token=eyJhbGciOiJIUzUxMiJ9.eyJpZCI6IjNhMzdmYmE3LTRhNjUtdmM4MS1iZTlhLTczOTg4MmQyZmRhZiIsImRhdGEiOnt9LCJyYW5kb20iOiJkODAsZmRkMTRhNjQyMzE3ZDAXYWY3MDFkOTgyNzAzYiJ9.D3pB5oTMRSCgzMARKuKdXDsvU11X7UXSWiZceoeNYcd7kqd1h7MYVlyDjiUdFX4PK0X0KNIjFoTXdSeC5yx4hA(10.5281/zenodo.17276778).)

2.2. Synthesis of Materials

2.2.1. Synthesis of HNT-NH₂. Two mL of APTES [(3-aminopropyl)triethoxysilane] and 10 mL of THP were added to 400 mg of HNT and stirred at 65 °C for 12 h. At the end of the reaction, the crude reaction mixture was centrifuged, and the solid was repeatedly washed with THP (3 × 5 mL) and then centrifuged to remove impurities. Finally, the solid was dried in an oven at 70 °C for 24 h to obtain 413 mg of HNT-NH₂.

2.2.2. Synthesis of HNT-NH₂-GSH. 150 mg of GSH were suspended in 12 mL of THP under a nitrogen atmosphere, to which 112 mg of EDC [1-ethyl-3(3-(dimethylamino)propyl) carbodiimide] were added, then left to stir for 10 min under a nitrogen atmosphere. At the end of this time, 200 mg of HNT-NH₂ and 5 mL of THP were added, and the resulting mixture was stirred for 48 h at room temperature under a nitrogen atmosphere. The crude reaction mixture was then centrifuged (at rt and 5000 rpm), and the solid obtained was washed with deionized water (3 × 5 mL) and finally dried under vacuum to obtain 220 mg of HNT-NH₂-GSH.

2.2.3. Synthesis of HNT-NH₂-GSH-Cu²⁺. To a dispersion of HNT-NH₂-GSH (100 mg) in H₂O (5 mL) was added CuCl₂ (50 mg).²⁹ The resulting mixture was stirred at 55 °C overnight. The reaction mixture was then centrifuged and washed several times with deionized H₂O to remove excess uncomplexed metal ions. The supernatant was removed, and the solid was dried under a vacuum to give 104 mg of product.

2.2.4. Synthesis of HNT-NH₂-GSH-Cu¹⁺. To a dispersion of HNT-NH₂-GSH (100 mg) in H₂O (5 mL) was added CuCl₂ (50 mg).²⁹ The resulting mixture was stirred at 55 °C overnight. To reduce Cu(II) to Cu(I) in the resulting HNT-NH₂-GSH-Cu²⁺ product, the sample was suspended in 6 mL of a 0.5 M ascorbic acid solution, which was then stirred for 3 h at room temperature. Finally, the suspension was centrifuged at 5300 rpm for 10 min, then washed three times with water. The supernatant was removed, and the solid was dried under vacuum to give 102 mg of product.

2.2.5. Procedure for Loading of Xanthopterin. 100 mg portion of HNT-NH₂-GSH-Cu¹⁺ was mixed with xanthopterin (10 mg) in an agate mortar. The physical mixture was then repeatedly ground until a homogeneous, opaque yellow final product (HNT-NH₂-GSH-Cu¹⁺-X) was obtained. To evaluate loading efficiency, we performed the same experiment as reported in our previous work.²⁸ A 10:1 (w/w) mixture of HNT-NH₂-GSH-Cu¹⁺ (25 mg) and xanthopterin (2.5 mg) was dispersed in 1 mL of DMSO and stirred continuously at room temperature overnight. The resulting suspension was centrifuged at 5300 rpm for 20 min, and the supernatant was analyzed by UV (Jasco V-730 spectrophotometer and quartz cuvettes with an optical path length of 1 cm).

2.3. Experimental Setup

2.3.1. General Procedure for the Solar Photocatalytic CO₂ Reduction. The photocatalytic tests were conducted at atmospheric pressure using a cylindrical batch Pyrex reactor filled with 0.1 g of sample, which was irradiated for 7 h with a solar lamp (Osram Ultra Vitalux 300 W, irradiance of 10.7 mW/cm²). A mixture of CO₂ (99.999%) and H₂ gas (evolved by an HK Hydrogen generator, purity 99.9996%) was flowed into the photoreactor to saturate the sample surface with the reagent molecules. With a mass flow controller, the H₂/CO₂ mixture was tuned to favor CO₂ methanation (H₂/CO₂ molar ratio 4:1).³⁰

The reaction products (under our experimental conditions, only CO and CH₄) were examined using an Agilent 8860 gas chromatograph (Carboxen column, TCD detector) and a Trace GC instrument (Porapak Q column, FID detector), both of which were adequately calibrated. The measurements were repeated three times (3% experimental error).

The CO₂ conversion values were calculated with eq 1

$$\text{CO}_2 \text{ conversion} \% = \left(\frac{\text{area}_{\text{peak CO}_2 \text{ in}} - \text{area}_{\text{peak CO}_2 \text{ out}} \times \left(\frac{\text{area}_{\text{peak standard in}}}{\text{area}_{\text{peak standard out}}} \right)}{\text{area}_{\text{peak CO}_2 \text{ in}}} \right) \times 100 \quad (1)$$

Moreover, the mass balance method was also applied, considering eq 2

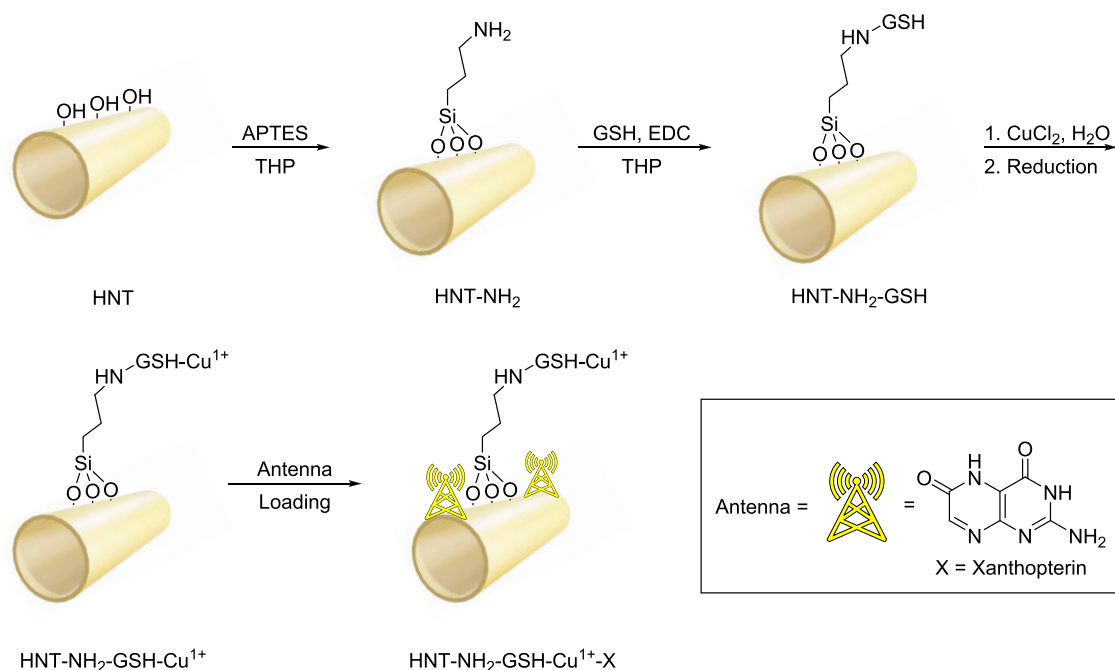
$$\text{CO}_2 \text{ conversion} \% = \left(\frac{\text{area}_{\text{peak CO}_2 \text{ out}}}{\text{area}_{\text{peak products out}} + \text{area}_{\text{peak CO}_2 \text{ out}}} \right) \times 100 \quad (2)$$

The two methods were in agreement ($\pm 5\%$, 95% reproducibility). The selectivity of the CO and CH₄ products on an electron basis was evaluated with eqs 3 and 4³¹

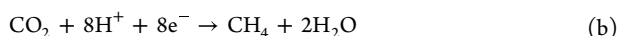
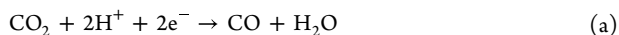
$$\text{CH}_4 \text{ selectivity} \% = \left(\frac{8N_{\text{CH}_4}}{(8N_{\text{CH}_4} + 2N_{\text{CO}})} \right) \times 100 \quad (3)$$

$$\text{CO selectivity} \% = \left(\frac{2N_{\text{CO}}}{(8N_{\text{CH}_4} + 2N_{\text{CO}})} \right) \times 100 \quad (4)$$

where N_{CH_4} and N_{CO} are the production rates of CH₄ and CO in $\mu\text{mol/g}_{\text{catalyst}} \cdot \text{h}_{\text{irradiation}}$, and the coefficients 8 and 2 are used to account for the electrons involved in the photocatalytic reduction reactions to

Scheme 1. Preparation of HNT-NH₂-GSH-Cu¹⁺-X

form CH₄ and CO from the CO₂ using H₂ as the electron donor and proton source, and considering the reactions (a) and (b).^{31–33}



The CH₄ yield (%) was calculated with eq 5

$$\text{CH}_4 \text{ yield \%} = \left(\frac{\text{CH}_4 \text{ selectivity \%} \times \text{CO}_2 \text{ conversion \%}}{100} \right) \quad (\text{5})$$

2.3.2. Electrochemical Measurements. Cyclovoltammetry (CV), linear sweep voltammetry (LSV), and differential pulse voltammetry (DPV) measurements were performed using a DropSens $\mu\text{Stat-i}$ 400s potentiostat/galvanostat equipped with Dropview 8400 software. A 0.1 M phosphate-buffered saline (PBS) solution (pH 7.4) was used for electrochemical measurements. CV tests were performed at a scan rate of 50 mV/s in the -0.2 – 1.0 V potential range. LSV tests were conducted using a 0.1 M PBS solution at a scan rate of 50 mV s⁻¹ within a 0–1.0 V potential range. Measurements were made using a commercial reference Screen-Printed Carbon Electrode (SPCE), from the Metrohm DropSens company, and a working SPCE modified with HNT-GSH-Cu (HNT-GSH-Cu/SPCE) by depositing on it (0.125 cm²) 25 μL of a suspension of HNT-GSH-Cu²⁺ (5 mg in 1 mL of distilled water). DPV tests were conducted using an optimized potential step (E_{step}) of 0.03 V, a potential pulse (E_{puls}) of 0.09 V, and a time pulse (T_{pul}) of 200 ms, with a scan rate of 40 mV/s in the 0.0–1.0 V potential range. Afterward, all measurements were repeated after the appropriate volumes (0.025–2.5 L) of a 10 mM bisphenol A solution were added to the 0.1 M PBS electrolyte solution (pH 7.4). The resulting sensors were dried at room temperature under a nitrogen atmosphere for 24 h.^{12,34} The sensor sensitivity (S) was always calculated (eq 6) as the ratio between the slope (m) of the calibration line and the geometric surface area (A) of the modified SPCE electrode (0.125 cm²).³⁵ The Limit of Detection (LOD) was calculated by the relationship between the standard deviation (SD) of the blank (solutions without any bisphenol A) and the slope (a) obtained from the calibration curve as follows (eq 7)³⁶

$$S = \frac{m}{A} \quad (\text{6})$$

$$\text{LOD} = 3.3 \times \frac{\text{SD}}{a} \quad (\text{7})$$

2.4. Characterization

2.4.1. Infrared Spectroscopy. FTIR-ATR analyses were conducted using an FTIR Agilent Cary 630 instrument equipped with an ATR sampling module. Thin films of the samples were applied to the ATR crystal and pressed gently. The results were derived from 512 scans acquired in the 4000–500 cm⁻¹ range with a resolution of 2 cm⁻¹ at room temperature.

2.4.2. Thermogravimetric Analysis. Thermal gravimetric analysis (TGA) was performed under 1 atm of prepurified nitrogen at a heating rate of 10 °C/min, in the temperature range of 50–900 °C. The instrument used is the PerkinElmer TGA 4000.

2.4.3. Evaluation of the Mean Particle Size and Polydispersity Index. To evaluate the mean particle size ($Z\text{-ave}$) and polydispersity index (PdI) of HNT, HNT-NH₂, HNT-NH₂-GSH, and HNT-NH₂-GSH-Cu²⁺, they were solubilized/suspended in water (1 mg/mL) and analyzed using Photon Correlation Spectroscopy (PCS) with a Zetasizer Nano S90 instrument (Malvern Instruments, Malvern, U.K.). The instrument was set to a detection angle of 90 °C and a 4 mW He–Ne laser operating at 633 nm with the temperature set to 25 °C. Three sets of measurements were used in the sample analysis, and the mean size \pm standard deviation (SD) was reported.

2.4.4. SEM-EDS. The synthesized material's morphology was analyzed by scanning electron microscopy using a Dual Beam Focused ion beam Versa 3D LoVac Dual Beam in secondary electron mode using a 5 keV electron beam. The samples were also analyzed in situ by using energy-dispersive X-ray spectroscopy (EDS) with a 20 keV electron beam. Before analysis, all samples were sputtered with 5 nm of Au to ensure proper conductivity during measurements.

2.4.5. UV-DRS. The ultraviolet visible-diffusion (UV–vis DRS) spectra were acquired using a Jasco V-670 instrument equipped with an integrating sphere, using BaSO₄ as reference.

2.4.6. Textural Properties. The textural properties of the samples were evaluated using N₂ physisorption measurements at -196 °C with a Micromeritics ASAP 2020 instrument after outgassing the samples overnight at 80 °C. The surface area of the samples was determined by the Brunauer–Emmett–Teller (BET) method. The pore size distribution was obtained using the Barrett–Joyner–Halenda (BJH) model (from the desorption curves).

2.4.7. X-ray Photoelectron. X-ray photoelectron spectra (XPS) were measured at a 45° takeoff angle relative to the surface sample holder, with a PHI 5000 Versa Probe II system (ULVAC-PHI, INC., base pressure of the main chamber 1×10^{-8} Pa).^{37,38} Samples were dispersed on a Si substrate and excited with the monochromatized Al $K\alpha$ X-ray radiation using a pass energy of 5.85 eV. The instrumental energy resolution was ≤ 0.5 eV. The XPS peak intensities were obtained after Shirley's background removal.^{37,38} Spectra calibration was achieved by fixing the Ag $3d_{5/2}$ peak of a clean sample at 368.3 eV.³⁹ The atomic concentration analysis was performed by considering the relevant atomic sensitivity factors. XP spectra were fitted with XPSPEAK4.1 software using Gaussian envelopes after background subtraction. This process involves data refinement utilizing the method of least-squares, which was continued until the highest possible correlation between the experimental spectrum and the theoretical profile was achieved. The residual or agreement factor R , defined by $R = [\sum (F_{\text{obs}} - F_{\text{calc}})^2 / \sum (F_{\text{obs}})^2]^{1/2}$, after minimization of the function $\sum (F_{\text{obs}} - F_{\text{calc}})^2$, converged to the value of 0.03.

3. RESULTS AND DISCUSSION

3.1. Synthesis

This work aims to utilize a sustainable, eco-biocompatible nanomaterial based on readily prepared natural materials for a sustainable application, such as the photoconversion of CO_2 into CH_4 . The entire synthetic process is further enhanced by the use of green solvents such as tetrahydropyran (THP)⁴⁰ and water, which are used in all synthetic steps (Scheme 1). The synthesis begins with the insertion of an amino termination using (3-aminopropyl)triethoxysilane (APTES) and the hydroxyl groups on the surface of HNT, with THP serving as the solvent. We then decided to conjugate GSH, a naturally occurring tripeptide, to serve as a chelator of Cu,^{41,42} which is helpful for the photoconversion of CO_2 . This was then reduced to Cu^+ in water in the presence of ascorbic acid. Finally, mimicking nature, an antenna, xanthopterin, also of natural origin, was loaded to increase the number of photons captured and enhance the photoconversion yield. This approach has previously been used by our research group²⁸ to improve the conversion yield of CO_2 to CH_4 by inserting xanthopterin, which, as wasps do,⁴³ captures more photons and enhances catalysis.

3.2. Characterizations

Successful functionalization was confirmed by FT-IR analysis. Figure 1 shows the FT-IR spectra of HNT, HNT-NH₂, and HNT-NH₂-GSH, demonstrating successful functionalization. The bands associated with the OH groups are visible in the HNT spectrum (black line): the Al–O–OH vibration is responsible for the peak at 907 cm^{-1} , while the stretching vibrations of the Al–OH groups are responsible for the bands at 3696 and 3624 cm^{-1} . In addition, a prominent O–Si–O peak is observed at approximately 1000 cm^{-1} , while the apical Si–O stretching mode is responsible for the peak at 749 cm^{-1} .^{5,15} In addition to these, there are signals related to functionalization with APTES (red line), namely the vibrational bands at 1500 – 1551 cm^{-1} , attributed to N–H deformation, and 1400 cm^{-1} due to the bending of C–H bonds in the carbon chain.⁴⁴ The blue line in Figure 1 shows the spectrum of the HNT-NH₂-GSH composite, in which an increase in the intensity of the above-mentioned signals in the 1500 – 1400 cm^{-1} range can be seen, and new signals in the 3000 – 2840 cm^{-1} region related to the stretching of C–H bonds typical of the GSH peptide chain and at 1390 cm^{-1} related to the C–N bond.^{23,44}

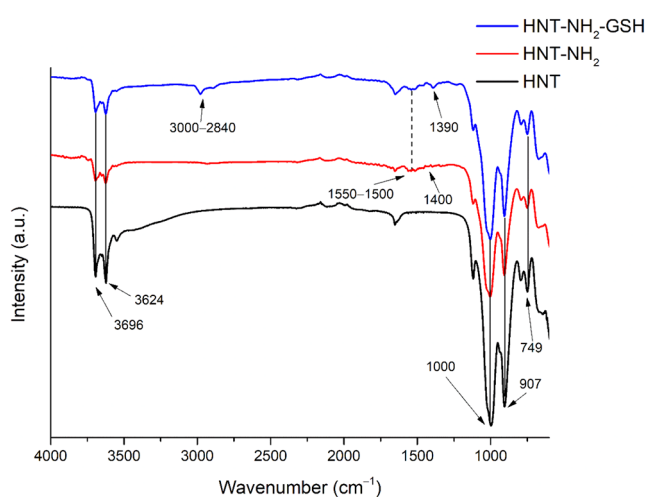


Figure 1. Stacked FT-IR spectra of HNT (black line), HNT-NH₂ (red line), and HNT-NH₂-GSH (blue line).

To verify the thermal properties, degree of functionalization (%f), and metal content of the synthesized nanocomposites, thermogravimetric analyses were performed.^{9,28} The overlapping thermograms of the various composites HNT (black line), HNT-NH₂ (red line), HNT-NH₂-GSH (blue line), HNT-NH₂-GSH-Cu¹⁺ (purple line), and HNT-NH₂-GSH-Cu²⁺ (green line) are shown in Figure 2.

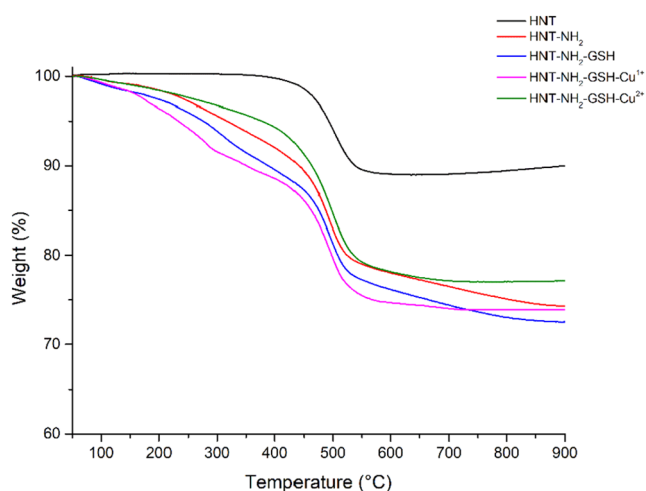


Figure 2. Thermogravimetric curves of HNT (black line), HNT-NH₂ (red line), HNT-NH₂-GSH (blue line), HNT-NH₂-GSH-Cu¹⁺ (purple line), and HNT-NH₂-GSH-Cu²⁺ (green line).

Table 1 shows the weight loss percentages of pristine HNT, HNT-NH₂, HNT-NH₂-GSH, and HNT-NH₂-GSH-Cu¹⁺. The degree of functionalization (%f) for the composite was calculated as reported in literature^{9,28} by considering the mass loss between 150 and $550 \text{ }^\circ\text{C}$. In particular, we note that %f for HNT-NH₂ is approximately 6%, while for HNT-NH₂-GSH it is approximately 7%. Finally, it was also possible to calculate the amount of metal by calculating the difference between the residue of HNT-NH-GSH and HNT-NH₂-GSH-Cu²⁺ or HNT-NH₂-GSH-Cu¹⁺, which is equal to 4.9% and 1.5 wt %, respectively.

The sizes of the aqueous suspensions of HNT, HNT-NH₂, HNT-NH₂-GSH, and HNT-NH₂-GSH-Cu²⁺ were analyzed by

Table 1. Mass Loss Percentages of Pristine HNT, HNT-NH₂, HNT-NH₂-GSH, HNT-NH₂-GSH-Cu²⁺, and HNT-NH₂-GSH-Cu¹⁺

sample	mass loss%				residue%	amount of metal%
	T < 150 °C	150 °C < T < 350 °C	350 °C < T < 550 °C	550 °C < T < 900 °C		
HNT	1.10	1.80	12.30	1.10	83.70	—
HNT-NH ₂	0.95	5.37	14.74	4.57	74.37	—
HNT-NH ₂ -GSH	1.78	7.20	14.06	4.55	72.41	—
HNT-NH ₂ -GSH-Cu ¹⁺	1.96	7.15	14.48	2.52	73.89	1.5
HNT-NH ₂ -GSH-Cu ²⁺	0.94	3.40	16.39	1.96	77.31	4.9

using PCS (Table 2). The results confirmed that HNT has dimensions in the micrometer range (1103 nm), consistent

Table 2. Mean Size (Z-ave) and Polydispersity Index (PDI) of HNT, HNT-NH₂, HNT-NH₂-GSH, HNT-NH₂-GSH-Cu²⁺

sample	Z-ave (nm) ± SD	PDI ± SD
HNT	1103 ± 131.2	0.598 ± 0.20
HNT-NH ₂	2299 ± 188.1	0.458 ± 0.05
HNTK-NH ₂ -GSH	4134 ± 628.6	0.863 ± 0.12
HNTK-NH ₂ -GSH-Cu ²⁺	2211 ± 199.5	0.330 ± 0.10

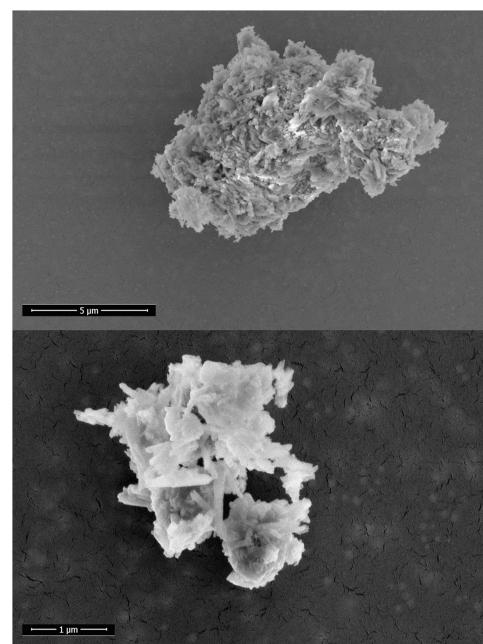
with reports in the literature.⁴⁵ Functionalization with APTES (NH₂) and subsequently with GSH increased the size to 2299 and 4134 nm, respectively. The presence of copper decreases the material's size by making the complex that forms more soluble and thus limiting the formation of aggregates, highlighting GSH chelation (2211 nm).^{18,46}

To calculate the amount of xanthopterin loaded by the nanosystem, the absorption spectra of 0.025 mg/mL xanthopterin in DMSO before and after loading were compared (Figure S1). From the comparison, it is clear that the absorption peak at 387 nm, characteristic of xanthopterin in DMSO, is completely depleted after the solution is shaken in the presence of the HNT-NH₂-GSH-Cu¹⁺-X nanocomposite. The disappearance of this band indicates that almost all xanthopterin has been effectively sequestered by the nanocomposite, achieving a loading efficiency of 99%.²⁸

The morphology of HNT-NH₂-GSH-Cu¹⁺-X was analyzed by using SEM measurements (Figure 3). The sample shows the typical tubular structure of halloysite nanotubes.^{9,17,28}

In conjunction with the SEM analyses, EDS measurements were performed. The element map shown in Figure 4 confirms the presence of all elements, such as C, N, S, and Cu, following the functionalization and loading of xanthopterin, together with those typical of HNT, namely, Si, Al, and O, as expected.

Figure S2 shows the XPS survey spectrum of HNT-NH₂-GSH-Cu¹⁺-X. Peaks corresponding to C 1s, O 1s, Si 2p, Al 2p, S 2p, and N 1s are evident, together with some additional peaks of other states of the same elements. High-resolution XPS of HNT-NH₂-GSH-Cu¹⁺-X was also performed in the C 1s, O 1s, Si 2p, Al 2p, S 2p, N 1s, and Cu 2p binding energy regions (Figure S3a–f). In particular, Figure S3e shows a peak at 99.7 eV with an evident shoulder at 100.2 eV due to the Si 2p spin-orbit components of the silicon substrate on which HNT-NH₂-GSH-Cu¹⁺-X was deposited for the XPS measurements. In addition, the broad band centered at about 103 eV is due to different Si–O states in halloysite (101.9 eV) and APTES (103.8 eV), as well as some SiO_x (102.8 eV) of the substrate surface on which the sample was deposited for XPS measurement (101.9 eV).^{47,48} The Al 2p band is at 74.0 eV, typical of Al₂O₃ states.⁴⁹ Surface functionalization with GSH is

**Figure 3. SEM micrograph of HNT-NH₂-GSH-Cu¹⁺-X.**

demonstrated by the presence of N 1s (398.9 eV) and S 2p (168.4 eV) states in an N/S = 0.9 ratio.

This latter spectrum, aside from the main peak, shows a lower-energy component at 165.6 eV due to the S–Cu(I) states.⁵⁰ The presence of a higher-energy component (168.6 eV) is likely due to the metal-driven Haber–Weiss reaction, which forms oxidized sulfur species that lead to sulfonic acid.⁵¹

Figure 5 shows the XP spectrum of HNT-NH₂-GSH-Cu¹⁺-X in the Cu 2p binding energy region. The Cu 2p_{3/2,1/2} main spin-orbit components are located at 932.1–951.9 eV with some lower components at 935.0–954.8 eV (spin-orbit coupling 19.8 eV). These energy values, together with the presence of a small satellite peak at 942.4 eV above the Cu 2p_{3/2} signal, confirm the presence of Cu(I) (relative intensity 89.9%) and a small quantity of Cu(II) (intensity relative 9.1%).^{52,53} Also, XPS atomic concentration analysis suggests an S/Cu surface ratio of 3.1.

3.3. Photocatalytic Activity

The synthesized nanomaterials were tested for solar CO₂ photocatalytic methanation. In our experimental conditions, only CO and CH₄ were found as the main products of the reaction. In Table 3, the experimental data obtained are reported, comparing the different nanocomposites. As expected, the sample without the Cu¹⁺ ions (bare HNT, HNT-X, HNT-NH₂, and HNT-NH₂-GSH) gave negligible activity (CO₂ conversion ≤5%) due to the absence of photocatalytically active sites (as the cuprous ions) able to

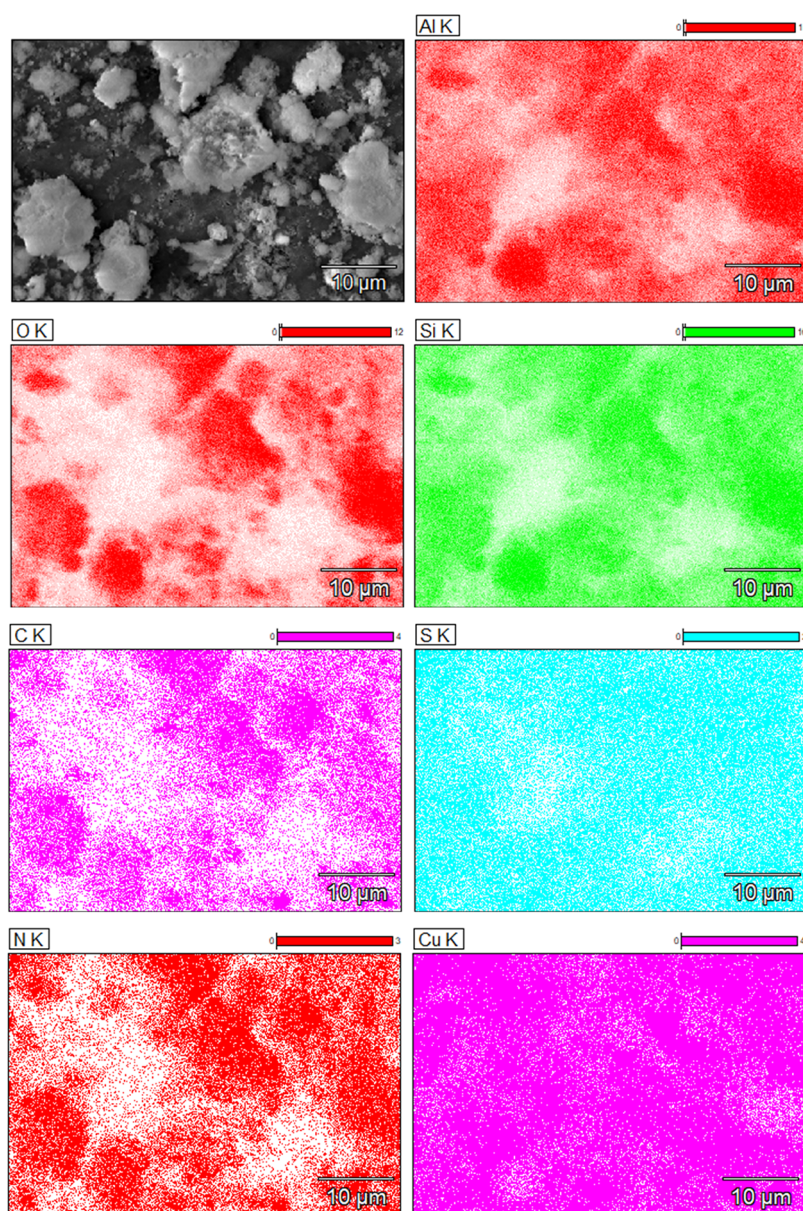


Figure 4. Energy-dispersive X-ray (EDS) mapping analysis of HNT-NH₂-GSH-Cu¹⁺.

promote the CO₂ reduction. As reported, the cuprous ions provided the necessary electrons to drive the reaction toward the selective formation of methane.^{31,32,54} The presence of only xanthopterin and HNT was not sufficient to photoconvert carbon dioxide.

Under solar light irradiation at moderate temperatures (45 °C in our case due to the heating of the used solar lamp), the H₂ molecules dissociate into hydrogen atoms on the surface of the active sites (metal). These hydrogen atoms hydrogenate adsorbed CO₂. In molecular metal complexes, direct catalytic oxidation of H₂ to H⁺ is promoted, thereby enhancing CO₂ conversion.^{30,33} For these reasons, the presence of metal active sites is fundamental. Subsequently, the generated H⁺ reacted with the adsorbed CO₂ at the basic sites of the HNT. The presence of the NH₂-GSH functionalization enabled efficient chelation of Cu(I) ions, exposing these species to the sample surface and allowing them to convert CO₂ into CH₄ and sequentially into methane.^{9,28} Indeed, the sample without this functionalization, HNT-Cu¹⁺ (Table 3, entry 2), showed low

photoactivity, confirming that the chelating action of GSH is crucial for promoting an efficient activation of the photocatalytic reaction on the cuprous ion sites. This indicated that interactions among all components of the compounds were necessary for successful CO₂ methanation. This synergistic effect between the several elements of the proposed green photocatalyst was further improved due to the presence of xanthopterin, which enhanced the harvesting of solar photons, resulting in optimal CO₂ conversion efficiency (42%) and enhancing the CH₄ selectivity (86%, CH₄ formation rate 7.98 μmol/g_{cat}·h) and yield (36%) (Table 3, entry 7).

Although it is very difficult to compare the obtained results with other ones investigated photocatalysts for the solar CO₂ methanation, due to the various experimental setups and conditions reported in the literature (such as the type of used lamp, duration of irradiation, temperature, pressure, etc.), the performance of the HNT-NH₂-GSH-Cu¹⁺-X sample is promising in terms of CH₄ formation rate, selectivity, and yield, considering that in the same experimental conditions, the

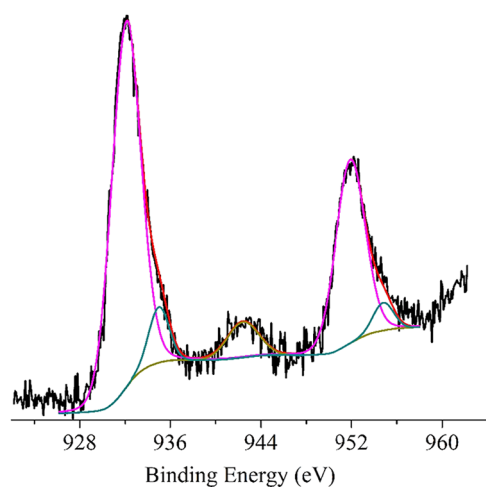


Figure 5. Al $K\alpha$ excited XPS of the HNT-NH₂-GSH-Cu¹⁺-X sample in the Cu 2p binding energy region: the magenta, dark cyan, and dark yellow lines refer to the 932.1, 935.0, and 942.4 eV Gaussian components, respectively. The blue line represents the background, and the red line superimposed on the experimental black profile refers to the sum of the Gaussian components.

standard Cu₂O/TiO₂-based semiconductor oxides exhibited a similar CO₂ conversion (45%), but favoring the CO formation 12 μmol/g_{cat}·h, with a selectivity of 67%, rather than the methane formation (5 μmol/g_{cat}·h CH₄ selectivity = 33%).⁵⁴ Indeed, with the here-examined HNT-NH₂-GSH-Cu¹⁺-X nanocatalyst, a higher CH₄ formation (7.98 μmol/g_{cat}·h) was achieved with higher selectivity (86%).

Higher CH₄ selectivity (up to 97%) can be achieved using other Cu₂O-based materials;⁵⁵ however, this comes at the cost of reduced biocompatibility and sustainability compared with our approach. Indeed, in the present work, Cu(I) ions are exclusively chelated within the hybrid sustainable composite structure, in contrast to the use of bare Cu₂O-based semiconductors, thereby improving the overall sustainability of the process.

For the best-performing nanocatalysts (HNT-NH₂-GSH, HNT-NH₂-GSH-Cu¹⁺, and HNT-NH₂-GSH-Cu¹⁺-X), the optical properties were evaluated by UV-DRS characterization (Figure S4). All of the nanomaterials exhibit a broad absorption band in the 250–350 nm range, attributed to the electronic transitions of GSH molecules.⁵⁶ The presence of Cu ions led to an additional feature in the 500–600 nm range, related to the localized surface plasmon resonance of copper.⁵⁷ This feature was more intense and red-shifted in the HNT-NH₂-GSH-Cu¹⁺-X sample due to the additional absorption

features of the xanthopterin antenna in the same visible light range.²⁸ This increased absorption in the visible range of the HNT-NH₂-GSH-Cu¹⁺-X nanocomposite improved the absorption and utilization of simulated solar light in the photocatalytic tests. Therefore, the combined action of the Cu ions and the antenna molecules enhanced the sample's solar photocatalytic performance, thereby improving it (Table 3, entry 7).

For the same samples, the textural properties were determined (Figure S5, Table S1). All of the examined nanocomposites exhibited a type IV isotherm with an H₂ hysteresis loop (Figure S5A), consistent with pores with wide bodies and narrow necks.⁵⁸ The addition of Cu ions and of the antenna molecule did not give substantial variations of the BET surface area (≈67–68 m²/g, Table S1), nor in the pore size distribution (Figure S5B), with a narrow distribution centered on mesopores of 10–11 nm. As expected, the textural properties were mainly determined by the presence of halloysite, the common support of all examined samples; therefore, no substantial variations were observed among the investigated nanomaterials.

Finally, Figure 6 reports the photocatalytic reusability of the best photocatalytically active sample, HNT-NH₂-GSH-Cu¹⁺-X,

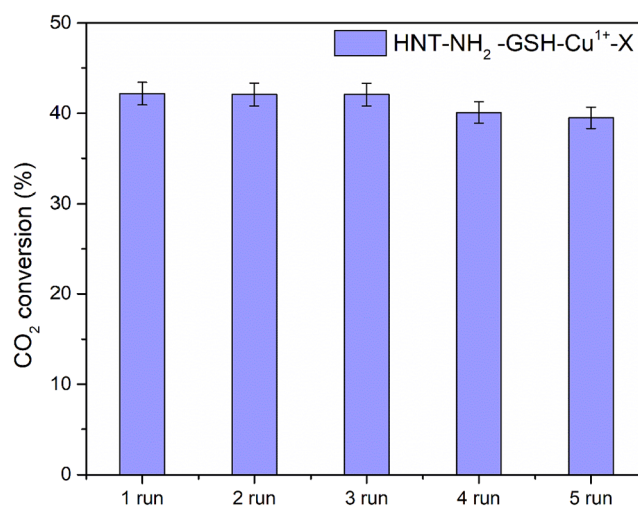


Figure 6. Photocatalytic runs (each run of 7 h of simulated solar irradiation) for the HNT-NH₂-GSH-Cu¹⁺-X photocatalyst in the CO₂ reduction reaction.

after five runs of the photocatalytic reaction (each run of 7 h of simulated solar irradiation). At the end of each run, the sample was flushed with He (30 cc/min) for 2 h to remove any

Table 3. Screening of Photocatalysts Used for the Photocatalytic CO₂ Reduction^a

entry	sample	CO ₂ conversion after 7 h of solar radiation (simulated)	CH ₄ selectivity	CO selectivity	CH ₄ yield	CH ₄ formation rate (μmol/g _{cat} ·h)	CO formation rate (μmol/g _{cat} ·h)
1	HNT	—	—	—	—	—	—
2	HNT-Cu ¹⁺	7.6%	57.1%	41.9%	4.3%	1.44	1.06
3	HNT-X	3.0%	—	—	—	—	—
4	HNT-NH ₂	—	—	—	—	—	—
5	HNT-NH ₂ -GSH	5.1%	12.2%	86.8%	0.6%	0.21	1.47
6	HNT-NH ₂ -GSH-Cu ¹⁺	11.3%	64.5%	34.5%	7.3%	1.60	0.86
7	HNT-NH ₂ -GSH-Cu ¹⁺ -X	42.2%	86.1%	12.9%	36.3%	7.98	1.20

^aReaction conditions: catalyst (100 mg), CO₂ and H₂ 1 atm, H₂/CO₂ molar ratio (4:1), 7 h of solar radiation (simulated), $T = 45$ °C, due to the heating of the solar lamp

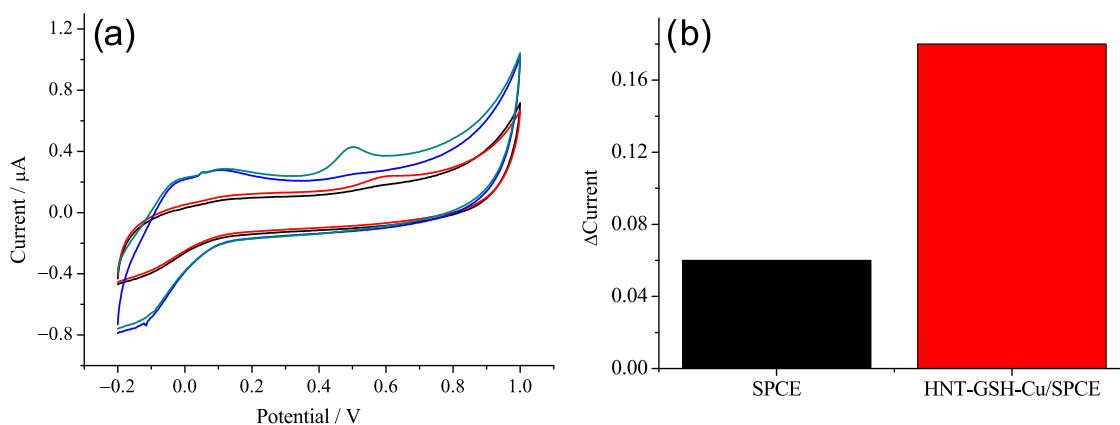


Figure 7. (a) Electrochemical behavior of SPCE (black and red lines), and HNT-NH₂-GSH-Cu²⁺/SPCE (blue and green lines) in $-0.2-1.0$ V potential range, before and after 250 nM of bisphenol A; (b) comparison between the responses.

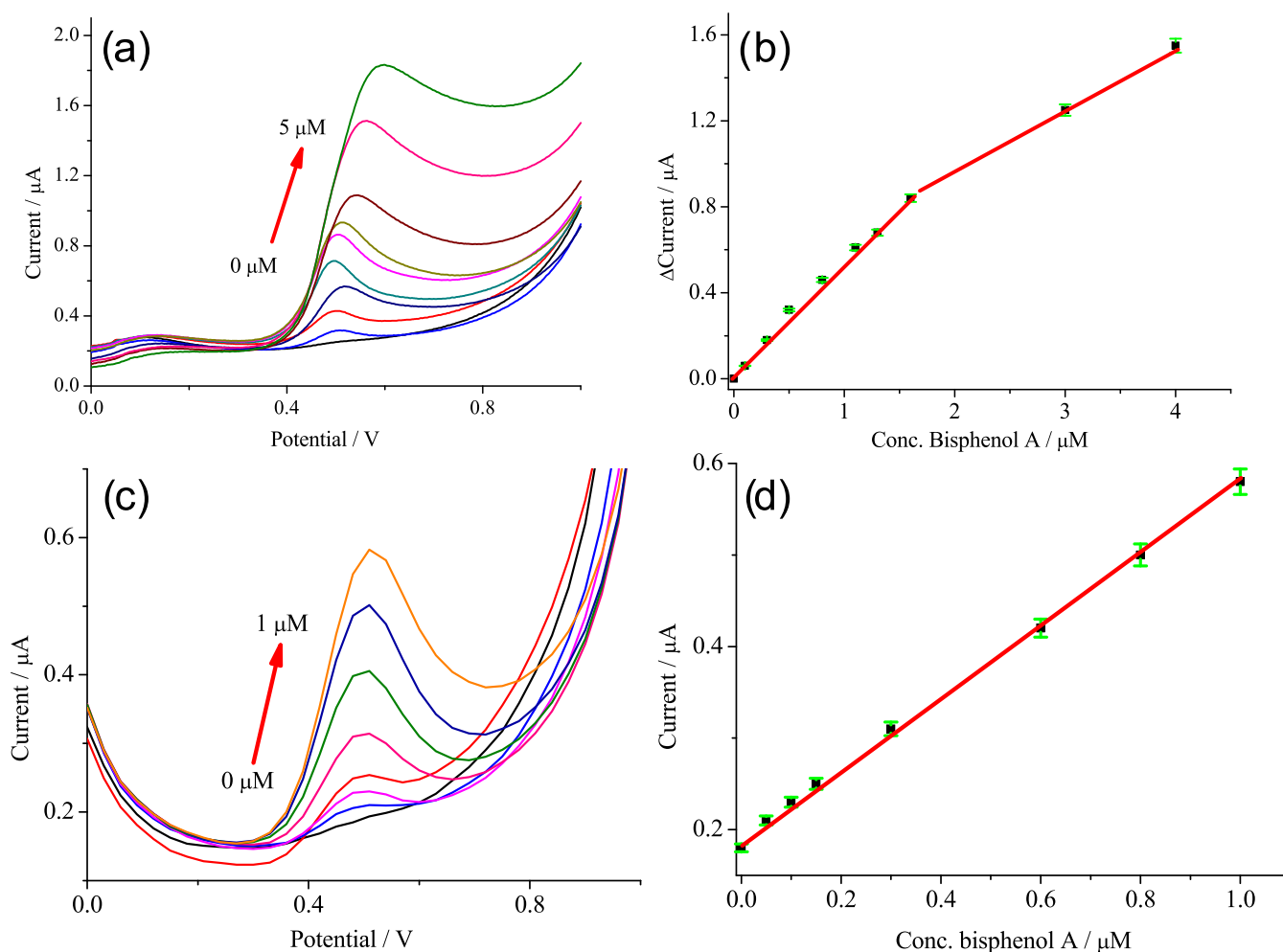


Figure 8. (a) LSV at different bisphenol A concentrations ($0-5 \mu\text{M}$, initial step $0.1 \mu\text{M}$) in 0.1 M PBS ($\text{pH } 7.4$); (b) calibration curve for anodic peak current (I_{pa}) vs the bisphenol A ($\text{RSD} \leq 2.1$ for five repeated whole cycles) (eq $y = a + b \times x$; $R^2 = 0.99763$; intercept = -0.00339 ± 0.00531 ; slope = 0.63729 ± 0.001794); (c) DPV at different bisphenol A concentrations ($0-1 \mu\text{M}$, initial step $0.05 \mu\text{M}$) in 0.1 M PBS ($\text{pH } 7.4$); (d) calibration curve for anodic peak current (I_{pa}) vs the bisphenol A concentration ($\text{RSD} \leq 1.8$ for five repeated whole cycles) (eq $y = a + b \times x$; $R^2 = 0.9926$; intercept = 0.18528 ± 0.00288 ; slope = 0.42264 ± 0.001823).

carbonaceous species physisorbed on the sample surface and to reuse the sample. The nanomaterial showed good stability, with only a slight decrease in the CO₂ conversion after the fourth run (i.e., 28 h of simulated solar irradiation). This little reduction in performance can be reasonably attributed to the

partial oxidation of Cu(I) into Cu(II), which are less active with respect to the cuprous ions.^{28,59,60} Despite this, the overall stability of HNT-NH₂-GSH-Cu¹⁺-X was optimal, indicating its potential for practical use in solar photocatalytic CO₂ conversion.

3.4. Sensor Activity

The sensing capabilities of bare SPCE and HNT-NH₂-GSH-Cu²⁺/SPCE were evaluated by CV analysis upon 250 nM bisphenol A (0.1 μL of a 10 mM solution of the bisphenol A added to 4 mL of a PBS 0.1 M electrolyte solution). Figure 7 shows the anodic oxidation peak (IPox) at approximately 0.6 and 0.5 V, for the SPCE and HNT-GSH-Cu²⁺/SPCE, respectively. The observed response for HNT-NH₂-GSH-Cu²⁺/SPCE is about three times as great as for SPCE. In addition, the shift to a lower peak potential and the increase in oxidation current imply faster electron-transfer kinetics in the HNT-NH₂-GSH-Cu²⁺/SPCE sensor.⁶¹

The detection capabilities of HNT-NH₂-GSH-Cu²⁺/SPCE were examined by LSV and DPV measurements (Figure 8a,c) using increasing bisphenol A concentrations. Figure 8b,d shows the related calibration curves. This nanosensor exhibits a sensitivity of 5.098 μA μM⁻¹ cm⁻², and an LOD of 0.022 μM, thus providing an excellent responsiveness to bisphenol A.

To highlight the importance of our nanocomposite for the electrochemical detection of bisphenol A, we present a comparative table of nanocomposite sensors reported in the literature (Table 4). It is easy to see why our composite is an

Table 4. Comparison of the Detection Performance of HNT-NH₂-GSH-Cu²⁺ and the Nanocomposite Sensors Reported for Bisphenol A

electrode materials	LOD μM	reference
HNT-NH ₂ -GSH-Cu ²⁺	0.022	this work
GCE/H-diA(6 mg)/C60(8 mg)	0.0014	62
MIP/CNTs-Au NPs/BOMC	0.005	63
SERS	0.003	64
NiCo-MOF/LPC-700/SPE	0.049	65
Ni-Cu(PDA)MOF/CNF/GC	0.075	66
Au@MIP	0.052	67
MIPPy/GQDs	0.040	68
carbon felt	0.480	69
exfoliated graphite (EG)	0.076	70
[Ru(bpy) ₃] ²⁺ on the ITO	0.029	71
MIP/Fe ₃ O ₄ NPs	0.380	72

excellent candidate as a sensor for detecting a contaminant, which is a significant concern at present. Although other nanosensors with lower LODs exist, the nanosensor described here is an excellent candidate due to its ease of preparation and the sustainability of its materials and processes.

5. CONCLUSIONS

This research successfully demonstrates the creation of a highly sustainable and effective multifunctional platform for simultaneous photocatalysis and electrochemical sensing. By leveraging natural and eco-biocompatible nanomaterials such as halloysite nanotubes, glutathione, and xanthopterin, and employing green synthetic methods, we have developed a nanocomposite that not only aligns with environmental sustainability principles but also delivers exceptional performance. The synergistic interplay among the HNT scaffold, the GSH chelating agent, the copper ions, and the xanthopterin antenna is crucial, as evidenced by the high CO₂ conversion and methane selectivity achieved under solar light. The nanomaterial's superior performance in CH₄ production compared to conventional photocatalysts highlights the advantages of this bioinspired approach. Additionally, the

same nanosystem exhibits impressive capabilities for detecting bisphenol A, confirming its versatility and potential for dual-purpose applications. This work provides a promising blueprint for designing next-generation, environmentally friendly nanomaterials that can address global challenges in energy and environmental protection in an integrated and efficient manner. In real-world scenarios, it could simultaneously contribute to CO₂ mitigation while providing sensitive monitoring of hazardous pollutants. Such versatility makes the nanosystems particularly attractive for industrial wastewater treatment, air quality monitoring, and sustainable energy production. Overall, the multifunctional design represents a significant step toward eco-friendly, cost-effective environmental technologies.

■ ASSOCIATED CONTENT

Supporting Information

The Supporting Information is available free of charge at <https://pubs.acs.org/doi/10.1021/acsanm.5c05781>.

Stacked UV spectra of xanthopterin (0.025 mg/mL in DMSO) and supernatant for the preparation of HNT-NH₂-GSH-Cu¹⁺ (Figure S1); Al-Kα excited XPS of HNT-NH₂-GSH-Cu¹⁺-X in the 0–1200 binding energy region (Figure S2); Al Kα excited XPS of the HNT-NH₂-GSH-Cu¹⁺-X samples in the in the: (a) C 1s binding energy region; (b) O 1s binding energy region; (c) N 1s binding energy region; (d) Al 2p binding energy region; (e) Si 2p binding energy region; (f) S 2p binding energy region (Figure S3); UV-DRS spectra of the examined samples (Figure S4); (A) N₂ isotherms and (B) pore size distribution of the examined samples (Figure S5); textural properties of the examined samples (Table S1) (PDF)

■ AUTHOR INFORMATION

Corresponding Authors

Vincenzo Patamia – Department of Drug and Health Sciences, University of Catania, 95125 Catania, Italy; orcid.org/0000-0002-0048-2631;
Email: vincenzo.patamia@unict.it

Giuseppe Floresta – Department of Drug and Health Sciences, University of Catania, 95125 Catania, Italy; orcid.org/0000-0002-0668-1260;
Email: giuseppe.floresta@unict.it

Authors

Erika Saccullo – Department of Drug and Health Sciences, University of Catania, 95125 Catania, Italy; Department of Biomedical and Biotechnological Sciences (Biometec), University of Catania, 95123 Catania, Italy

Angelo Ferlazzo – Department of Chemical Sciences, University of Catania, 95125 Catania, Italy; orcid.org/0000-0003-2844-1441

Giusy Dativo – Department of Chemical Sciences, University of Catania, 95125 Catania, Italy

Roberto Fiorenza – Department of Chemical Sciences, University of Catania, 95125 Catania, Italy

Giulia Sambataro – Department of Drug and Health Sciences, University of Catania, 95125 Catania, Italy

Elena Bruno – Department of Physics and Astronomy "Ettore Majorana", University of Catania, 95123 Catania, Italy; CNR-IMM, 95123 Catania, Italy

Antonino Gulino – Department of Chemical Sciences,
University of Catania, 95125 Catania, Italy
Antonio Rescifina – Department of Drug and Health Sciences,
University of Catania, 95125 Catania, Italy; orcid.org/0000-0001-5039-2151

Complete contact information is available at:
<https://pubs.acs.org/10.1021/acsanm.5c05781>

Notes

The authors declare no competing financial interest.

ACKNOWLEDGMENTS

The research leading to these results has received funding from the European Union—NextGenerationEU through the Italian Ministry of University and Research under PNRR—M4C2—11.3 Project PE_00000019 “HEAL ITALIA” (Antonio Rescifina, Vincenzo Patamia, and Erika Saccullo), CUP E63C22002080006. Giusy Dativo thanks the Sicilian Micro and Nano Technology Research and Innovation Center (SAMOTHRACE, CUP E63C22000900006) for funding the Ph.D. grant. The views and opinions expressed are those of the authors only and do not necessarily reflect those of the European Union or the European Commission. Neither the European Union nor the European Commission can be held responsible for them. The authors wish to thank the Bionanotech Research and Innovation Tower at the University of Catania for access to the Dual Beam FIB and the Zetasizer Nano S90.

REFERENCES

- (1) Liu, W.-J.; Jiang, H.; Yu, H.-Q. Development of biochar-based functional materials: toward a sustainable platform carbon material. *Chem. Rev.* **2015**, *115*, 12251–12285.
- (2) Moura, B.; Rosero-Romo, J.; Monteiro, H.; Alberto, A.; Laranjeira, J.; Martin-Iglesias, S.; Silvan, U.; Lanceros-Mendez, S.; Salazar, D.; Martins, C. Addressing safety and sustainability issues in the development of nano-enabled MULTI-FUNCTIONAL materials for metal additive manufacturing. *Sustainable Mater. Technol.* **2024**, *41*, No. e01085.
- (3) Irimia-Vladu, M. Green electronics: biodegradable and biocompatible materials and devices for a sustainable future. *Chem. Soc. Rev.* **2014**, *43*, 588–610.
- (4) Han, W. B.; Yang, S. M.; Rajaram, K.; Hwang, S. W. Materials and Fabrication Strategies for Biocompatible and Biodegradable Conductive Polymer Composites toward Bio-Integrated Electronic Systems. *Adv. Sustainable Syst.* **2022**, *6*, No. 2100075.
- (5) Patamia, V.; Fiorenza, R.; Zagni, C.; Agustin-Salazar, S.; Scirè, S.; Floresta, G.; Rescifina, A. TiO₂/Loofah–Halloysite Bio–Hybrid Composites as Efficient Systems for VOCs Removal. *Chem. - Eur. J.* **2024**, *30*, No. e202304276.
- (6) Saccullo, E.; Patamia, V.; Bifarella, A.; Ferlazzo, A.; Fiorenza, R.; Spitaleri, L.; Sfuncia, G.; Nicotra, G.; Zagni, C.; Iapichino, M. T. A.; et al. Conversion of VOC-derived CO₂ into sustainable products with a natural magnetic alginate composite. *Int. J. Biol. Macromol.* **2025**, *304*, No. 140695.
- (7) Patamia, V.; Saccullo, E.; Magaletti, F.; Fuochi, V.; Furnari, S.; Fiorenza, R.; Furneri, P. M.; Barbera, V.; Floresta, G.; Rescifina, A. Nature-inspired innovation: Alginate-kojic acid material for sustainable antibacterial and carbon dioxide fixation. *Int. J. Biol. Macromol.* **2024**, *277*, No. 134514.
- (8) Massaro, M.; Colletti, C.; Lazzara, G.; Milioto, S.; Noto, R.; Riela, S. Halloysite nanotubes as support for metal-based catalysts. *J. Mater. Chem. A* **2017**, *5*, 13276–13293.
- (9) Saccullo, E.; Patamia, V.; Magaletti, F.; Dativo, G.; Camarda, M.; Fiorenza, R.; Barbera, V.; Floresta, G.; Rescifina, A. Halloysite-kojic acid conjugate: A sustainable material for the photocatalytic CO₂ reduction and fixation for cyclic carbonates production. *J. CO₂ Util.* **2024**, *85*, No. 102865.
- (10) Failla, M.; Ferlazzo, A.; Abbate, V.; Neri, G.; Saccullo, E.; Gulino, A.; Rescifina, A.; Patamia, V.; Floresta, G. THP as a sensor for the electrochemical detection of H₂O₂. *Bioorg. Chem.* **2024**, *152*, No. 107721.
- (11) Heras, J. Y.; Rodriguez, S. D.; Negri, R. M.; Battaglini, F. Chelating electrodes as taste sensor for the trace assessment of metal ions. *Sens. Actuators, B* **2010**, *145*, 726–733.
- (12) Ferlazzo, A.; Chelly, M.; Gulino, A.; Neri, G. Biosensing of Urea with a Functionalized Gold Electrode for Health and Food Monitoring. *J. Agric. Food Chem.* **2025**, *73* (40), 25628–25635, DOI: 10.1021/acs.jafc.5c08426.
- (13) Jia, F.; Liu, Q.; Chen, Z.; Wei, W. Colorimetric determination of nine metal ions based on the de-aggregation of papain-functionalized gold nanoparticles and using three chelating agents. *Microchim. Acta* **2019**, *186*, No. 854.
- (14) Lauriane, N.; Najih, R.; Chtaini, A. Electrochemical sensor of heavy metals based on chelating compounds. *Pharm. Anal. Acta* **2014**, *5*, No. 2.
- (15) Patamia, V.; Fiorenza, R.; Brullo, I.; Marsala, M. Z.; Balsamo, S. A.; Distefano, A.; Furneri, P. M.; Barbera, V.; Scirè, S.; Rescifina, A. A sustainable porous composite material based on loofah-halloysite for gas adsorption and drug delivery. *Mater. Chem. Front.* **2022**, *6*, 2233–2243.
- (16) Sadjadi, S. Halloysite-based hybrids/composites in catalysis. *Appl. Clay Sci.* **2020**, *189*, No. 105537.
- (17) Patamia, V.; Zagni, C.; Fiorenza, R.; Fuochi, V.; Dattilo, S.; Riccobene, P. M.; Furneri, P. M.; Floresta, G.; Rescifina, A. Total Bio-Based Material for Drug Delivery and Iron Chelation to Fight Cancer through Antimicrobial Activity. *Nanomaterials* **2023**, *13*, No. 2036.
- (18) Ferlazzo, A.; Iapichino, M. T. A.; Calabrese, G.; D’Accurso, G.; Fiorenza, R.; Pistarà, V.; Gulino, A.; Rescifina, A.; Patamia, V.; Floresta, G. Nanosensors Made of Halloysite and Kojic Acid Metal Complexes for Dopamine Detection. *ACS Appl. Nano Mater.* **2025**, *8*, 16736–16747, DOI: 10.1021/acsanm.5c02759.
- (19) Goda, E. S.; Gab-Allah, M.; Singu, B. S.; Yoon, K. R. Halloysite nanotubes based electrochemical sensors: A review. *Microchem. J.* **2019**, *147*, 1083–1096.
- (20) Jeamjumnunja, K.; Cheycharoen, O.; Phongzithiganna, N.; Hannongbua, S.; Prasittichai, C. Surface-modified halloysite nanotubes as electrochemical CO₂ sensors. *ACS Appl. Nano Mater.* **2021**, *4*, 3686–3695.
- (21) Meng, S.-L.; Li, J.-H.; Ye, C.; Yin, Y.-L.; Zhang, X.-L.; Zhang, C.; Li, X.-B.; Tung, C.-H.; Wu, L.-Z. Concurrent Ammonia Synthesis and Alcohol Oxidation Boosted by Glutathione-Capped Quantum Dots under Visible Light. *Adv. Mater.* **2024**, *36*, No. 2311982.
- (22) Wang, W.; Wang, T.; Chen, S.; Lv, Y.; Salmon, L.; Espuche, B.; Moya, S.; Morozova, O.; Yun, Y.; Di Silvio, D. Cu (I)-Glutathione Assembly Supported on ZIF-8 as Robust and Efficient Catalyst for Mild CO₂ Conversions. *Angew. Chem.* **2024**, *136*, No. e202407430.
- (23) Cui, X.; Wang, J.; Liu, B.; Ling, S.; Long, R.; Xiong, Y. Turning Au Nanoclusters Catalytically Active for Visible-Light-Driven CO₂ Reduction through Bridging Ligands. *J. Am. Chem. Soc.* **2018**, *140*, 16514–16520.
- (24) Bagherpour, S.; Pérez-García, L. Recent advances on nanomaterial-based glutathione sensors. *J. Mater. Chem. B* **2024**, *12*, 8285–8309, DOI: 10.1039/D4TB01114G.
- (25) Han, Q.; Shen, X.; Zhu, W.; Zhu, C.; Zhou, X.; Jiang, H. Magnetic sensing film based on Fe₃O₄@ Au-GSH molecularly imprinted polymers for the electrochemical detection of estradiol. *Biosens. Bioelectron.* **2016**, *79*, 180–186.
- (26) Ai, L.; Liu, Z.; Zhang, X.; Wang, L.; Jia, D.; Guo, N.; Zha, M.; Tan, C. Engineering cycling of Cu²⁺/Cu⁺ pairs in Bi₂WO₆ nanoflowers for boosting photocatalytic CO₂ reduction. *J. Colloid Interface Sci.* **2025**, *692*, No. 137480.
- (27) Mao, Y.; Zhang, M.; Zhai, G.; Si, S.; Liu, D.; Song, K.; Liu, Y.; Wang, Z.; Zheng, Z.; Wang, P.; et al. Asymmetric Cu (I)–W Dual-

Atomic Sites Enable C–C Coupling for Selective Photocatalytic CO₂ Reduction to C₂H₄. *Adv. Sci.* **2024**, *11*, No. 2401933.

(28) Saccullo, E.; Dativo, G.; Lombardo, R.; Iapichino, M. T. A.; Fiorenza, R.; Patamia, V.; Floresta, G. Natural antenna molecule in halloysite-kojic acid composite for the solar photocatalytic CO₂ methanation. *Mater. Today Chem.* **2025**, *44*, No. 102587.

(29) Xiong, J.; Wang, Y.; Xue, Q.; Wu, X. Synthesis of highly stable dispersions of nanosized copper particles using L-ascorbic acid. *Green Chem.* **2011**, *13*, 900–904.

(30) Chen, Y.; Zhang, Y.; Fan, G.; Song, L.; Jia, G.; Huang, H.; Ouyang, S.; Ye, J.; Li, Z.; Zou, Z. Cooperative catalysis coupling photo-/photothermal effect to drive Sabatier reaction with unprecedented conversion and selectivity. *Joule* **2021**, *5*, 3235–3251.

(31) Long, R.; Li, Y.; Liu, Y.; Chen, S.; Zheng, X.; Gao, C.; He, C.; Chen, N.; Qi, Z.; Song, L.; et al. Isolation of Cu atoms in Pd lattice: forming highly selective sites for photocatalytic conversion of CO₂ to CH₄. *J. Am. Chem. Soc.* **2017**, *139*, 4486–4492.

(32) Fiorenza, R.; Bellardita, M.; Balsamo, S. A.; Spitaleri, L.; Gulino, A.; Condorelli, M.; D'Urso, L.; Scire, S.; Palmisano, L. A solar photothermocatalytic approach for the CO₂ conversion: Investigation of different synergisms on CoO–CuO/brookite TiO₂–CeO₂ catalysts. *Chem. Eng. J.* **2022**, *428*, No. 131249.

(33) Zhang, P.; Sui, X.; Wang, Y.; Wang, Z.; Zhao, J.; Wen, N.; Chen, H.; Huang, H.; Zhang, Z.; Yuan, R.; et al. Surface Ru–H bipyridine complexes-grafted TiO₂ nanohybrids for efficient photocatalytic CO₂ methanation. *J. Am. Chem. Soc.* **2023**, *145*, 5769–5777.

(34) Ferlazzo, A.; Gulino, A.; Neri, G. Scandia-doped zirconia for the electrochemical detection of hazardous dihydroxybenzene (DHB) isomers in water. *Environ. Sci.: Adv.* **2024**, *3*, 1392–1399.

(35) Maugeri, L.; Fangano, G.; Ferlazzo, A.; Forte, G.; Gulino, A.; Petralia, S. A DNA biosensor integrating surface hybridization, thermo-responsive coating, laminar-flow technology and localized photothermal effect for efficient electrochemical detection of nucleic acids. *Sens. Diagn.* **2024**, *3*, 1966–1975.

(36) Abid, K.; Ferlazzo, A.; Neri, G. Graphene quantum dots (GQDs)-modified screen-printed electrode for the determination of cannabidiol (CBD) in hemp seeds flour. *FlatChem* **2024**, *46*, No. 100673.

(37) Briggs, D.; Grant, J. *Surface Analysis by Auger and X-Ray Photoelectron Spectroscopy*; IMP: Chichester, UK, 2003.

(38) Gulino, A. Structural and electronic characterization of self-assembled molecular nanoarchitectures by X-ray photoelectron spectroscopy. *Anal. Bioanal. Chem.* **2013**, *405*, 1479–1495.

(39) Greczynski, G.; Hultman, L. Compromising science by ignorant instrument calibration—need to revisit half a century of published XPS data. *Angew. Chem., Int. Ed.* **2020**, *59*, 5002–5006.

(40) Dastidar, R. G.; Kim, M. S.; Zhou, P.; Luo, Z.; Shi, C.; Barnett, K. J.; McClelland, D. J.; Chen, E. Y.-X.; Van Lehn, R. C.; Huber, G. W. Catalytic production of tetrahydropyran (THP): a biomass-derived, economically competitive solvent with demonstrated use in plastic dissolution. *Green Chem.* **2022**, *24*, 9101–9113.

(41) Shi, Y.; Sun, K.; Shan, J.; Li, H.; Gao, J.; Chen, Z.; Sun, C.; Shuai, Y.; Wang, Z. Selective CO₂ Electromethanation on Surface-Modified Cu Catalyst by Local Microenvironment Modulation. *ACS Catal.* **2022**, *12*, 8252–8258.

(42) Wang, W.; Wang, T.; Chen, S.; Lv, Y.; Salmon, L.; Espuche, B.; Moya, S.; Morozova, O.; Yun, Y.; Di Silvio, D.; Daro, N.; Berlande, M.; Hapiot, P.; Pozzo, J.-L.; Yu, H.; Hamon, J.-R.; Astruc, D. Cu(I)-Glutathione Assembly Supported on ZIF-8 as Robust and Efficient Catalyst for Mild CO₂ Conversions. *Angew. Chem., Int. Ed.* **2024**, *63*, No. e202407430.

(43) Plotkin, M.; Volynchik, S.; Ermakov, N. Y.; Benyamini, A.; Boiko, Y.; Bergman, D. J.; Ishay, J. S. Xanthopterin in the oriental hornet (*Vespa orientalis*): light absorbance is increased with maturation of yellow pigment granules. *Photochem. Photobiol.* **2009**, *85*, 955–961.

(44) Peixoto, A. F.; Fernandes, A. C.; Pereira, C.; Pires, J.; Freire, C. Physicochemical characterization of organosilylated halloysite clay nanotubes. *Microporous Mesoporous Mater.* **2016**, *219*, 145–154.

(45) Vergaro, V.; Abdullayev, E.; Lvov, Y. M.; Zeitoun, A.; Cingolani, R.; Rinaldi, R.; Leporatti, S. Cytocompatibility and uptake of halloysite clay nanotubes. *Biomacromolecules* **2010**, *11*, 820–826.

(46) Wu, D.; Delair, T. Stabilization of chitosan/hyaluronan colloidal polyelectrolyte complexes in physiological conditions. *Carbohydr. Polym.* **2015**, *119*, 149–158.

(47) Gulino, A.; Lupo, F.; Condorelli, G. G.; Fragalà, M. E.; Amato, M. E.; Scarlata, G. Reversible photoswitching of stimuli-responsive Si (100) surfaces engineered with an assembled 1-cyano-1-phenyl-2-[4'-(10-undecenyloxy) phenyl]-ethylene monolayer. *J. Mater. Chem.* **2008**, *18*, S011–S018.

(48) Gulino, A.; Condorelli, G. G.; Mineo, P.; Fragalà, I. An x-ray photoelectron spectra and atomic force microscopy characterization of silicasubstrates engineered with a covalently assembled siloxane monolayer. *Nanotechnology* **2005**, *16*, No. 2170.

(49) Cristaldi, D. A.; Fortuna, C. G.; Gulino, A. A photoelectron spectroscopy study of lava stones. *Anal. Methods* **2013**, *5*, 3458–3462.

(50) Florio, F.; Ferlazzo, A.; Bonforte, S.; Nicotra, G.; Neri, G.; Pinkas, I.; van der Boom, M. E.; Gulino, A. Unveiling the sensing ability of new MoS₂ nanoparticles: from fundamental insights into practical applications for nitrites. *J. Mater. Chem. C* **2025**, *13*, 11214–11222, DOI: 10.1039/D5TC01165E.

(51) Weser, U. Redox reactions of sulphur-containing amino-acid residues in proteins and metalloproteins, an XPS study. In *Cation Ordering and Electron Transfer, Structure and Bonding*; Springer, 2007; pp 145–160 DOI: 10.1007/bfb0111194.

(52) Ferlazzo, A.; Bonforte, S.; Florio, F.; Petralia, S.; Sorace, L.; Muzzi, B.; Caneschi, A.; Gulino, A. Photochemical eco-friendly synthesis of photothermal and emissive copper nanoclusters in water: towards sustainable nanomaterials. *Mater. Adv.* **2024**, *5*, 8034–8041.

(53) Kaminker, R.; De Hatten, X.; Lahav, M.; Lupo, F.; Gulino, A.; Evmenenko, G.; Dutta, P.; Browne, C.; Nitschke, J. R.; Van Der Boom, M. E. Assembly of surface-confined homochiral helicates: chiral discrimination of DOPA and unidirectional charge transfer. *J. Am. Chem. Soc.* **2013**, *135*, 17052–17059.

(54) Fiorenza, R.; Contarino, C.; Spano, V.; Iapichino, M. T. A.; Balsamo, S. A. Photothermo-catalytic strategies for the CO₂ valorisation using TiO₂-based composites. *Catal. Today* **2023**, *423*, No. 114251.

(55) Deng, Y.; Wan, C.; Li, C.; Wang, Y.; Mu, X.; Liu, W.; Huang, Y.; Wong, P. K.; Ye, L. Synergy effect between facet and zero-valent copper for selectivity photocatalytic methane formation from CO₂. *ACS Catal.* **2022**, *12*, 4526–4533.

(56) Singh, G.; Dogra, S. D.; Kaur, S.; Tripathi, S.; Prakash, S.; Rai, B.; Saini, G. Structure and vibrations of glutathione studied by vibrational spectroscopy and density functional theory. *Spectrochim. Acta, Part A* **2015**, *149*, 505–515.

(57) Popok, V. N.; Novikov, S. M.; Lebedinskij, Y. Y.; Markeev, A. M.; Andreev, A. A.; Trunkin, I. N.; Arsenin, A. V.; Volkov, V. S. Gas-aggregated copper nanoparticles with long-term plasmon resonance stability. *Plasmonics* **2021**, *16*, 333–340.

(58) Thommes, M.; Kaneko, K.; Neimark, A. V.; Olivier, J. P.; Rodriguez-Reinoso, F.; Rouquerol, J.; Sing, K. S. W. Physisorption of gases, with special reference to the evaluation of surface area and pore size distribution (IUPAC Technical Report). *Pure Appl. Chem.* **2015**, *87*, 1051–1069.

(59) Fiorenza, R.; Bellardita, M.; Balsamo, S. A.; Gulino, A.; Condorelli, M.; Compagnini, G.; Scirè, S.; Palmisano, L. A solar photothermo-catalytic combined process for the VOCs combustion and the subsequent CO₂ valorization using noble metal-free catalysts. *Catal. Today* **2023**, *413-415*, No. 113949.

(60) Celaya, C. A.; Delesma, C.; Torres-Arellano, S.; Sebastian, P.; Muniz, J. Understanding CO₂ conversion into hydrocarbons via a photoreductive process supported on the Cu₂O (1 0 0), (1 1 0) and (1 1 1) surface facets: A first principles study. *Fuel* **2021**, *306*, No. 121643.

(61) Ferlazzo, A.; Espro, C.; Iannazzo, D.; Bonavita, A.; Neri, G. Yttria-zirconia electrochemical sensor for the detection of tyrosine. *Mater. Today Commun.* **2023**, *35*, No. 106036.

- (62) Tchieno, F. M. M.; Dmitrieva, E.; Boye, S.; Schiemenz, S.; Kluge, R. Diamine@halloysite/C60 composite-based Bisphenol A electrochemical sensor. *J. Electroanal. Chem.* **2023**, *943*, No. 117593.
- (63) Hu, X.; Feng, Y.; Wang, H.; Zhao, F.; Zeng, B. A novel bisphenol A electrochemical sensor based on a molecularly imprinted polymer/carbon nanotubes-Au nanoparticles/boron-doped ordered mesoporous carbon composite. *Anal. Methods* **2018**, *10*, 4543–4548.
- (64) Li, S.; He, D.; Li, S.; Chen, R.; Peng, Y.; Li, S.; Han, D.; Wang, Y.; Qin, K.; Ren, S.; Chen, P.; Gao, Z. Magnetic Halloysite Nanotube-Based SERS Biosensor Enhanced with Au@Ag Core–Shell Nanotags for Bisphenol A Determination. *Biosensors* **2022**, *12*, No. 387.
- (65) Wang, Y.; Liu, Z.; Zhao, Z.; Fei, M.; Xie, Y.; Guo, H.; Zhao, P.; Fei, J. Modulation of metal centers of MOF in-situ grown on lignin-derived carbon to enhance adsorption capacity and electrochemical sensing performance for bisphenol A. *Chem. Eng. J.* **2024**, *499*, No. 156279.
- (66) Dey, B.; Ahmad, M. W.; Al-Shannaq, R.; Al-Humaidi, J. Y.; Hossain, S. K. S.; Patra, C. N.; Althomali, R. H.; Rahman, M. M.; Choudhury, A. Non-Enzymatic Electrochemical Sensing of Bisphenol A in Drinking Water and Milk Using Bimetallic Nickel-Copper Metal–Organic Framework. *J. Anal. Test.* **2024**, *8*, 451–465.
- (67) Han, E.; Pan, Y.; Li, L.; Cai, J. Bisphenol A detection based on nano gold-doped molecular imprinting electrochemical sensor with enhanced sensitivity. *Food Chem.* **2023**, *426*, No. 136608.
- (68) Tan, F.; Cong, L.; Li, X.; Zhao, Q.; Zhao, H.; Quan, X.; Chen, J. An electrochemical sensor based on molecularly imprinted polypyrrole/graphene quantum dots composite for detection of bisphenol A in water samples. *Sens. Actuators, B* **2016**, *233*, 599–606.
- (69) Kim, M.; Song, Y. E.; Xiong, J.-Q.; Kim, K.-Y.; Jang, M.; Jeon, B.-H.; Kim, J. R. Electrochemical detection and simultaneous removal of endocrine disruptor, bisphenol A using a carbon felt electrode. *J. Electroanal. Chem.* **2021**, *880*, No. 114907.
- (70) Ndlovu, T.; Arotiba, O. A.; Sampath, S.; Krause, R. W.; Mamba, B. B. An Exfoliated Graphite-Based Bisphenol A Electrochemical Sensor. *Sensors* **2012**, *12*, 11601–11611.
- (71) Li, Q.; Li, H.; Du, G.-F.; Xu, Z.-H. Electrochemical detection of bisphenol A mediated by [Ru(bpy)₃]²⁺ on an ITO electrode. *J. Hazard. Mater.* **2010**, *180*, 703–709.
- (72) Kaassamani, R. A.; Sawan, S.; Jaffrezic-Renault, N.; Maalouf, R. A novel electrochemical sensor based on iron oxide nanoparticles coated with molecularly imprinted polymers for Bisphenol A detection. *Microchem. J.* **2025**, *208*, No. 112632.



CAS BIOFINDER DISCOVERY PLATFORM™

CAS BIOFINDER HELPS YOU FIND YOUR NEXT BREAKTHROUGH FASTER

Navigate pathways, targets, and
diseases with precision

Explore CAS BioFinder

